

Properties of hypermassive neutron stars formed in mergers of spinning binaries

Wolfgang Kastaun^{1,2} and Filippo Galeazzi³

¹*Physics Department, University of Trento, via Sommarive 14, I-38123 Trento, Italy*

²*Max-Planck-Institut für Gravitationsphysik, Albert Einstein Institut, Am Mühlenberg 1, 14476 Potsdam, Germany*

³*Institut für Theoretische Physik, Max-von-Laue-Straße 1, 60438 Frankfurt, Germany*

We present numerical simulations of binary neutron star mergers, comparing irrotational binaries to binaries of NSs rotating aligned to the orbital angular momentum. For the first time, we study spinning BNSs employing nuclear physics equations of state, namely the ones of Lattimer and Swesty as well as Shen, Horowitz, and Teige. We study mainly equal mass systems leading to a hypermassive neutron star (HMNS), and analyze in detail its structure and dynamics. In order to exclude gauge artifacts, we introduce a novel coordinate system used for post-processing. The results for our equal mass models show that the strong radial oscillations of the HMNS modulate the instantaneous frequency of the gravitational wave (GW) signal to an extent that leads to separate peaks in the corresponding Fourier spectrum. In particular, the high frequency peaks which are often attributed to combination frequencies can also be caused by the modulation of the $m = 2$ mode frequency in the merger phase. As a consequence for GW data analysis, the offset of the high frequency peak does not necessarily carry information about the radial oscillation frequency. Further, the low frequency peak in our simulations is dominated by the contribution of the plunge and the first 1–2 bounces. The amplitude of the radial oscillations depends on the initial NS spin, which therefore has a complicated influence on the spectrum. Another important result is that HMNSs can consist of a slowly rotating core with an extended, massive envelope rotating close to Keplerian velocity, contrary to the common notion that a rapidly rotating core is necessary to prevent a prompt collapse. Finally, our estimates on the amount of unbound matter show a dependency on the initial NS spin, explained by the influence of the latter on the amplitude of radial oscillations, which in turn cause shock waves.

PACS numbers: 04.25.dk, 04.30.Db, 04.40.Dg, 95.30.Sf

I. INTRODUCTION

Relativistic numerical simulations of binary neutron star (BNS) mergers are bringing the fate of the remnant object into increased focus (see e.g. [1–11] and references therein). Such simulations have revealed that hyper- (or supra-) massive neutron stars (HMNS; see [12] for precise definitions) are the most likely outcomes of BNS mergers with equations of state (EOS) that allow a maximum mass for non-rotating neutron stars (NS) in the range $2.6\text{--}2.8 M_{\odot}$.

Among the plethora of interesting physics that can be extracted from the numerical analysis, the understanding of the features encoded in the gravitational radiation produced by the complex dynamics of the HMNS is perhaps the chief motivation driving most simulations. The prospects for detecting such signals with ground-based laser interferometers are continuously improving, see [13–15]. The study of the gravitational radiation frequency spectra of HMNS might in particular open the possibility of inferring the masses and radii of neutron stars through common techniques of asteroseismology [2, 4, 11, 16, 17], a long-standing issue in relativistic astrophysics. The extraction of two mode frequencies through a successful gravitational wave (GW) detection might help to further tighten existing constraints on the EOS for high-density matter, such as the recent observations [18, 19] of $\sim 2 M_{\odot}$ neutron stars.

Important steps in this direction were taken by [2] who studied the oscillation modes of the HMNS as an isolated gravitating fluid. It was found that the fluid oscillations correspond directly to peaks in the GW spectrum, in which the most salient feature is the quadrupole ($m = 2$) oscillation mode which appears as a triplet, with side bands caused by the

non-linear coupling to the fundamental quasi-radial ($m = 0$) mode. However, this interpretation implies oscillations with essentially fixed frequencies. During the plunge and merger phase however, the system is still highly non-linear. As already pointed out in [9], this often results in strong modulations of the mode frequencies themselves. We will show that the high frequency peak does not necessarily correspond to a combination frequency, but can also be caused directly by the $m = 2$ perturbations during the merger phase, where the frequency shortly reaches higher values.

A more recent study [11] has focused on the low-frequency peak of the spectrum, showing that it satisfies an essentially universal relation with the compactness of the stars in the binary so that a robust method to constrain the EOS can be derived by combining the information from the two peaks. The low frequency peak was interpreted in [11] as the result of a double core structure during the merger. We support that view by proving that the low frequency peak in our simulations is due to the GW signal during the plunge and the first bounces.

In contrast to binary black hole (BH) mergers, only few simulations investigate the influence of the initial NS spin [20–22]. The reason is that consistent initial data for spinning NS binaries has become available only recently [23]. In our previous work [22], we successfully used approximated initial data for spinning binaries, which we also employ here. In contrast to existing studies which assume simplified analytic EOSs, we evolve spinning binaries with nuclear physics EOSs. In [22], we studied the influence of the NS spin on the spin of the BH. In this work, we also provide some data points for models with nuclear physics EOSs. Our main focus is however on the cases where a HMNS is formed. In [21], a dependency of the $m = 2$ mode frequency on the ini-

tial NS spin was discovered. We investigate the impact on the GW spectrum in more detail, revealing a complicated picture which makes it difficult to deduce the spin from the GW signal.

We also investigate the influence of the initial NS spin on the ejected matter for the first time. The amount, composition, and temperature of matter ejected in BNS mergers is of considerable astrophysical interest since r -process nucleosynthesis in the ejected matter is one explanation for the abundance of heavy elements in the universe. Our study does not include neutrino radiation and hence cannot provide realistic values for the composition of ejected matter. However, our estimates indicate a significant impact of the spin on the amount of ejected matter, mediated by the influence on the radial oscillation amplitude.

A very important quantity in BNS merger simulations is the threshold mass above which the merger results in a prompt collapse to a BH. In particular, current models linking BNS mergers to short gamma ray bursts require the formation of a BH. In [7], the threshold mass was computed for a wide range of EOSs, using the conformal flatness approximation. We confirm those results in full GR for the two EOS considered in our work.

A related question is what exactly prevents the immediate collapse of HMNSs to a BH. The exact contributions of differential rotation and/or thermal effects are still largely unconstrained. It is known that isolated NSs can support large masses if they follow a j -const rotation law for which the core rotates more rapidly [12]. Such configurations are the standard model for HMNSs formed in mergers. Some results presented in [24] on the other hand indicate a slower central rotation rate. In this paper we study the rotation profiles in detail and show that HMNSs can indeed exhibit a rotation profile where the core rotates slowly, while the outer layers rotate only slightly below Kepler velocity. The question whether the core or the outer layers stabilize a HMNS is important for estimating the lifetime. For example, it was shown in [5] that an artificial cooling mechanism acting on the whole system can reduce the lifetime of HMNSs (with a simplified analytic EOS). Neutrino cooling on the other hand will probably have a stronger effect on the outer, optically thin layers of a HMNS. The rotation profile is also important for models describing the amplification of the magnetic field (which is not included in our work), such as [25, 26].

The paper is organized as follows: Sec. II describes technical details of our simulations such as the computational framework and a novel coordinate system used for post-processing. Our binary NS models are described in Sec. III. The results of our simulations are presented in Sec. IV. In particular, Sec. IV A summarizes the inspiral phase and the outcome of the merger, Sec. IV B addresses the structure and evolution of the HMNSs, Sec. IV C relates the GW signals and spectra to the dynamics of the HMNS, and Sec. IV D is dedicated to matter ejection. Finally, a summary and a discussion is provided in Sec. V.

II. NUMERICAL METHODS

A. Evolution framework

All simulations in this work rely on the `WhiskyThermal` code described in [27, 28] to evolve the general relativistic hydrodynamics equations (see also [29]). The code implements finite-volume, high-resolution shock-capturing methods, and makes use of nuclear physics EOSs in tabulated form, including thermal and composition effects. We do not include neutrino radiation in our study, and simply advect the electron fraction together with the fluid.

The spacetime is evolved by the `McLachlan` code [30], which is part of the publicly available Einstein Toolkit [31]. All codes are based on the `Cactus` computational framework. The `McLachlan` code employs high order finite-difference methods and offers different options for the formulation of the Einstein equations. Instead of the popular BSSNOK formulation [32–34], we chose the CCZ4 formulation described in [28, 35] because of its constraint-damping abilities.

As gauge conditions, we apply the “ $1 + \log$ ”-slicing condition [36] for the lapse function together with the hyperbolic $\bar{\Gamma}$ -driver condition [37] for the shift vector. At the outer edge of the computational domain, we employ Sommerfeld radiative boundary conditions for the spacetime. Furthermore, we enforce reflection symmetry with respect to the orbital plane. We do however not enforce π -symmetry, to avoid suppressing potential physical instabilities.

Our simulations make use of moving box mesh refinement, provided by the `Carpet` code [38]. In detail, we use six refinement levels during the inspiral, with the two finest ones tracking the movement of the NSs. Close to the merger, when the moving refinement regions are overlapping, they are replaced with fixed refinement regions fully containing the previous ones. When a collapse to a BH is imminent, we activate another refinement level in order to improve the accuracy of the BH properties. To ascertain numerical accuracy of the evolution framework, we rely on the tests already performed in [27, 28], which include an expensive convergence test of a binary merger simulation.

We detect the formation of apparent horizons utilizing the module `AHFinderDirect` [39] from the Einstein toolkit. Mass and spin of the BH are computed by means of the isolated horizon formalism [40, 41] implemented in the `QuasiLocalMeasures` module. In order to extract the GW signal, we decompose the Weyl scalar Ψ_4 into multipole moments on spheres of fixed coordinate radius. Computing the gravitational wave strain then requires twofold integration in time. In order to filter out the typical drift of the numerical waveform due to the cumulative effect of small numerical errors, we use the fixed frequency integration technique described in [42], with a cut frequency of 500 Hz. Since we are mainly interested in the GW spectra, we refrain from extrapolating the waveforms to infinity and use a finite extraction radius near the outer boundary of the computational domain.

B. Computing initial data

The initial data for the irrotational binary models in this work is computed using the publicly available LORENE code [43]. To obtain properties of corresponding isolated, uniformly and differentially rotating stars, we make use of the RNS code [44].

In order to compute binaries with spin, we manually add a rotational velocity field to irrotational models. This is done as described in [22], by scaling the residual velocity field in the co-orbiting frame according to

$$\vec{w} = (1 - s) \vec{w}_L + s \vec{\Omega} \times \vec{x}. \quad (1)$$

Above, $w^i = u^i/u^0$, u^μ is the fluid 4-velocity, $\vec{\Omega}$ is the orbital angular velocity vector, \vec{w}_L is the original irrotational velocity field, and s is a free parameter that determines the amount of spin.

In contrast to the method described in [23], our recipe for adding spin violates the constraint equations of GR. Thanks to the constraint-damping CCZ4 evolution scheme [35], the constraint violation becomes sufficiently small during the first millisecond of evolution, as detailed in [28]. The constraint violations do however render the definition of the initial angular momentum ambiguous. We use a definition of ADM angular momentum given by Eq. (68) in [43], which takes the form of a volume integral over fluid quantities, and which is very similar to the Newtonian expression. Finally, we note that the modified rotational velocity profile does not satisfy hydrostatic equilibrium and thus introduces oscillations. For the spins considered here, the resulting oscillation amplitude is however less than 1% in terms of the central density and can be safely ignored.

C. Coordinates for analysis

For our analysis of HMNS properties such as multipole moments and rotation rates, we treat the system as a perturbation of a stationary, axisymmetric, and asymptotically flat background. To this end, we require a more suitable coordinate system than the one used in our simulations. The main problem with the latter is that even when the system approaches an axisymmetric state after the merger, the spatial coordinates do not reflect this, because the gauge conditions employed in the evolution are not designed to seek symmetries. In terms of proper distance axis ratios, the coordinate circles exhibit a deformation comparable with the physical deformation of the HMNS. Moreover, this deformation oscillates. The time slicing on the other hand is less problematic, judging by the lapse function which becomes reasonably stationary.

For those reasons, we construct a new coordinate system on each time slice in a postprocessing step. For simplicity, we restrict ourselves to the orbital plane (the equatorial symmetry plane). The new polar coordinates (r, ϕ) are defined in terms of the following requirements:

1. The origin is the center of the π -symmetry of our models.

2. Radial coordinate lines are parametrized by proper arc length, i.e., $g_{rr} = 1$.
3. The ϕ -coordinate along constant r is proportional to proper arc length, i.e., $g_{\phi\phi, \phi} = 0$.
4. Along each circle $r = \text{const}$, the radial and polar coordinate lines are on average orthogonal, i.e.,

$$\int_{-\pi}^{\pi} g_{r\phi}(r, \phi) d\phi = 0. \quad (2)$$

5. The shift vector β^i of the new coordinates approaches zero for large radii.

To show that such coordinates exist, one can treat the coordinate circles as a foliation of the orbital plane, with a radial lapse function and a shift vector (not to be confused with the lapse and shift of the 3+1-decomposition). Requirement 2 leads to an algebraic expression for the lapse in terms of the shift. Requirement 3 yields an ordinary scalar differential equation of first order for the shift. After taking the periodic boundary condition into account, the solutions still possess one free parameter, which is fixed by requirement 4. Requirement 5 reduces the remaining freedom of a constant global rotation on each timeslice to a rotation that is also constant in time, and which is irrelevant for our analysis.

To compute the above coordinates numerically, we use an iterative method acting on the whole coordinate system at once. Each iteration consists of the following substeps, which each enforce one of the requirements, but preserve the others only when the solution is reached:

1. Compute the proper arclength of radial lines, and use it as the new radial coordinate.
2. Compute the proper arclength along the coordinate circles $l(r, \phi) = \int_0^\phi d\phi' \sqrt{g_{\phi\phi}(r, \phi')}$ as well as the circumferential radius $2\pi r_c(r) = l(r, 2\pi)$. Using this, we then define a new ϕ -coordinate $\phi \rightarrow l(r, \phi)/r_c(r)$.
3. Apply the mapping $\phi \rightarrow \phi + \delta\phi(r)$, where $\delta\phi(r)$ fulfills the condition

$$\frac{d}{dr} \delta\phi = -\frac{1}{2\pi r_c^2} \int_{-\pi}^{\pi} g_{r\phi} d\phi. \quad (3)$$

4. Apply a global rotation such that the $\phi = 0$ coordinate is aligned with the x -axis at the outer edge of the computational domain.

We stop iterating as soon as, *during each substep*, the coordinates change less than a prescribed fraction (typically 0.1) of the grid resolution. As initial guess for the iteration, we apply the canonical mapping to polar coordinates from the Cartesian simulation coordinates. As a test, we mapped the Euclidean plane to strongly warped initial coordinates, and successfully recovered standard polar coordinates.

We use the new coordinates to define moments for any quantity q over a domain of radius R by

$$P_m^q = \int_0^R \int_0^{2\pi} q(r, \phi) e^{im\phi} dA, \quad (4)$$

$$p_m^q(r) = \frac{1}{2\pi} \int_0^{2\pi} q(r, \phi) e^{im\phi} d\phi, \quad (5)$$

where the proper area form dA is given by

$$dA = \sqrt{g_{rr}g_{\phi\phi} - g_{r\phi}^2} dr d\phi = \sqrt{r_c^2 - g_{r\phi}^2} dr d\phi. \quad (6)$$

For an axisymmetric manifold one can show that $g_{r\phi} = 0$, the radial coordinate r is the Riemannian distance function¹, and the radial coordinate lines are geodesics. Together with the condition $g_{\phi\phi, \phi} = 0$, we find that ∂_ϕ is a Killing vector. Hence, for solutions axisymmetric around the origin, all moments P_m and $p_m(r)$ of physical quantities vanish unless $m = 0$. Naturally, the moments above are not useful if the NS is not centered around the coordinate origin. For this reason, we do not use the framework for unequal-mass models in this work.

Next, we define a fluid angular velocity by

$$\Omega(t, r, \phi) = \frac{\partial\phi}{\partial x^b} (\alpha v^b - \bar{\beta}^b). \quad (7)$$

Here, α is the lapse function, x^b denotes the simulation coordinates, and v^b the fluid 3-velocity. $\bar{\beta}^b$ is the shift vector corresponding to the new coordinates, related to the shift vector β^b of the simulation coordinates by

$$\bar{\beta}^b = \beta^b + \frac{\partial \bar{x}^b}{\partial t}, \quad (8)$$

where \bar{x}^b are the new coordinates in terms of the old ones. We note that in the limit of a stationary and axisymmetric space-time, $\bar{\beta}^\phi$ is a measure of the frame dragging, and Ω is the angular frequency as observed from infinity. Further, rigid rotation is equivalent to $\Omega = \text{const}$. Also note that even in the limit of large radii, points of constant r, ϕ can be subject to acceleration, because the proper distance to the origin also depends on the geometry in the strong field region. For this reason, we prefer to use the circumferential radius r_c , which depends on the geometry at smaller radii less directly, via the shape of coordinate spheres.

Figure 1 shows the new coordinates for one of our simulations shortly after the merger. In comparison, the simulation coordinates exhibit a dominant $m = 2$ distortion as well as a spiral deformation. The deformation remains mostly stationary after the merger, with a slight wobbling synchronized to the oscillations of the HMNS. At late times, the physical deformations of the HMNS we want to measure become smaller

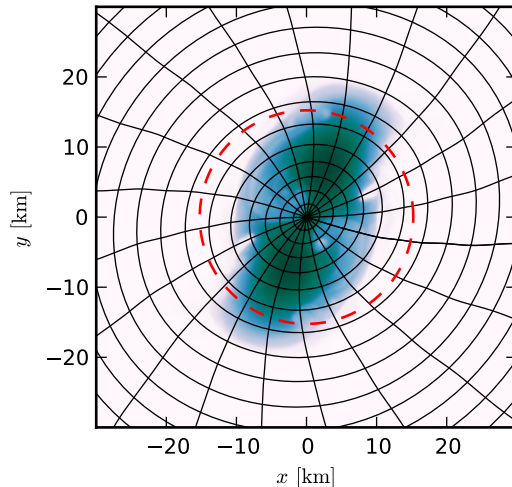


FIG. 1. The polar coordinate system constructed for analysis at a time 0.9 ms after the merger, for model SHT-M2.0-I. The black radial lines are the coordinate lines of constant ϕ , and the black circles mark coordinate lines of constant r_c . Both are spaced equidistantly. For comparison, we show the density profile as color plot, and a coordinate circle with respect to simulation coordinates (dashed red curve).

than the coordinate deformation. For the models considered in this work, the deformations of the coordinates mainly affect the $m = 2$ and $m = 4$ moment amplitudes and phase velocities. This can be seen in Fig. 2, where we compare the amplitude $|P_2^\rho|$ computed using the new coordinates to values obtained using the canonic polar coordinates associated with the Cartesian simulation coordinates. The (complex valued) moment acquires a constant offset when using the simulation coordinates, which leads to a modulation of the moments absolute value even if the physical amplitude of the NS oscillation remains constant. For $m = 0$ moments like average rotation rate or radius, the differences turn out to be minor in our simulations. Still, the new coordinates are useful to exclude gauge effects. We conclude that the transformation to well defined coordinates is essential to get reliable values for multipole moments of HMNSs and suppress gauge artifacts.

III. MODELS

For the simulations presented in this work, we consider two different nuclear physics EOSs which incorporate thermal effects and composition (electron fraction). One is the Lattimer-Swesty (LS) EOS [45], which is based on a compressible liquid drop model with Skyrme interaction [46]. We use the variant with incompressibility modulus $K = 220$ MeV. The other one is the Shen-Horowitz-Teige (SHT) EOS (see [47, 48]), which is derived from a relativistic mean-field model for uniform matter with a modified NL3 set of interaction parameters. To construct initial data, we assume cold matter at β -equilibrium.

¹ We note that using the exponential map to construct coordinates is not a good choice in general. Even if the injectivity radius is larger than the computational domain, which is not always the case, $g_{\phi\phi}$ will vary strongly, which renders the multipole moments meaningless.

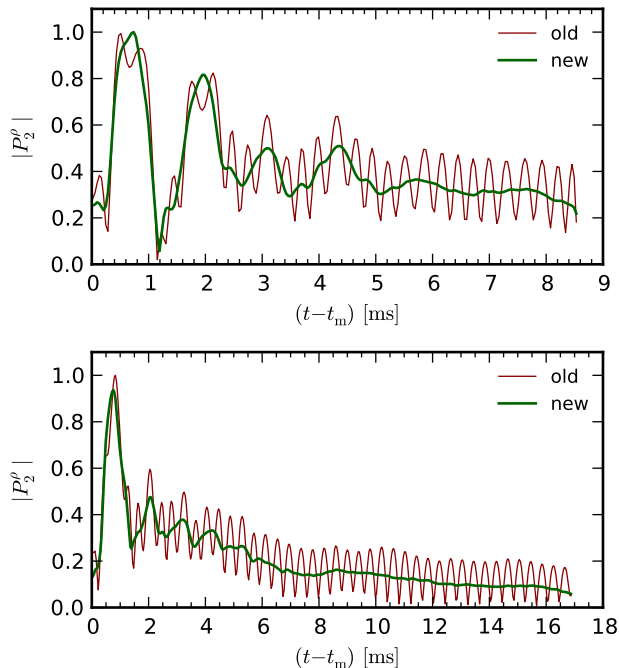


FIG. 2. Comparison of density moments P_2^ρ computed either using the new coordinate system (thick green line) or the simulation coordinates (thin red line). Shown are the results for models LS220-M1.5-I (top panel) and SHT-M2.0-I (bottom panel).

We study several irrotational equal-mass binaries with different total mass. In addition, we evolve two of the equal-mass binaries with NS spins aligned to the orbital angular momentum. We also report results for one unequal-mass irrotational binary (we note this model was still evolved using the BSS-NOK instead of the CCZ4 formulation). All our models are summarized in Table I.

To quantify the NS spin, we compute the change ΔJ_{ADM} of total ADM angular momentum (see also [22]) of the binary with respect to the irrotational model of same baryonic mass and separation. The NS spins in Table I are given in terms of the frequency $2\pi\Delta F_{\text{R}} = \frac{1}{2}\Delta J_{\text{ADM}}/I_\infty$, where I_∞ is the moment of inertia of the nonrotating NS in isolation. Compared to the rotation rate of 44.05 Hz observed for the well known double pulsar PSR J0737-3039 A, the chosen values for the spinup ΔF_{R} are larger, but they are still small compared to the Kepler limit. The latter is reached at a rotation rate of 893 Hz for models LS220-M1.5-I and -S, and 814 Hz for models SHT-M2.0-I and -S. The spinup corresponds to an increase ≈ 0.1 of the dimensionless spin $\Delta\chi_{\text{NS}} = \frac{1}{2}\Delta J_{\text{ADM}}/M_\infty^2$, where M_∞ is the gravitational mass of the NS in isolation.

The initial separations are large enough to allow 6–11 orbits until merger. The total baryonic mass is chosen around the threshold mass for prompt BH collapse given in [7], since we are mainly interested in models which lead to a stable HMNS or delayed collapse. For comparison, the maximum baryonic mass of cold nonrotating stars is $M_{\text{B}} = 2.42 M_\odot$ for the LS EOS and $M_{\text{B}} = 3.38 M_\odot$ for the SHT EOS. The maximum

Model	$M_{\text{B}}[M_\odot]$	$M_\infty[M_\odot]$	$\Delta F_{\text{R}}[\text{Hz}]$	$\Omega_{\text{o}}[\text{rad/s}]$	$d[\text{km}]$
SHT-M2.0-I	4.01	1.80	0	1460	74.2
SHT-M2.0-S	4.01	1.80	155.4	1460	74.2
SHT-M2.2-I	4.39	1.95	0	1505	76.0
LS220-M1.5-I	3.12	1.41	0	1552	64.5
LS220-M1.5-S	3.12	1.41	159.8	1552	64.5
LS220-M1.7-I	3.46	1.54	0	1611	66.2
LS220-M1.8-I	3.62	1.61	0	1636	66.9
LS220-M1.4-U	2.94	1.26, 1.41	0	1520	63.3

TABLE I. Parameters of the binary NS models. M_{B} is the total baryonic mass of the binary (Baryonic masses are based on a formal baryon mass of $m_{\text{B}} = 931.494 \text{ MeV}$ throughout this work). M_∞ is the gravitational mass of each star at infinite separation. Ω_{o} is the initial orbital angular velocity, and d the initial proper distance between density maxima locations. ΔF_{R} is the NSs rotation rate compared to the irrotational case (see main text).

mass of rigidly rotating stars is $M_{\text{B}} = 2.83 M_\odot$ and $M_{\text{B}} = 3.97 M_\odot$, respectively.

The setup of the numerical grid is identical for spinning and irrotational models, and the finest grid resolution is 295 m for all models. The outer boundaries of the numerical domain are located a 803 km for the LS220 models, and 945 km for the SHT models.

IV. RESULTS

In this section we present the outcome of our numerical simulations. For a discussion of the numerical accuracy of spinning BNS simulations using the same code, we refer the reader to [28], while the particularities of using tabulated EOSs are discussed in [27].

A. Inspiral phase and merger outcome

To measure the orbital trajectories, we use the positions of the rest mass density maximum with respect to the coordinates defined in Sec. II C. The proper separation for the equal-mass models is estimated from the radial coordinate (which equals the proper distance along radial coordinate lines), and the orbital phase is defined as the ϕ -coordinate. Figure 3 shows the proper distance versus the orbital phase. To compare different models, we align the phase at a separation of $d = 20 M_\infty$, where finite size effects should still be small. In units of the NS gravitational mass, the separations are indeed very similar up to this point, as it would be the case for point particles. The differences are comparable to the eccentricity caused by the inaccuracies of the initial data. For smaller separations, shown in the inset of Fig. 3, the discrepancies between the models increase, as finite size effects become more and more significant. We did not try to relate the orbital trajectories to models of tidal effects. However, we do observe an influence of the NS spin. When comparing spinning and irrotational

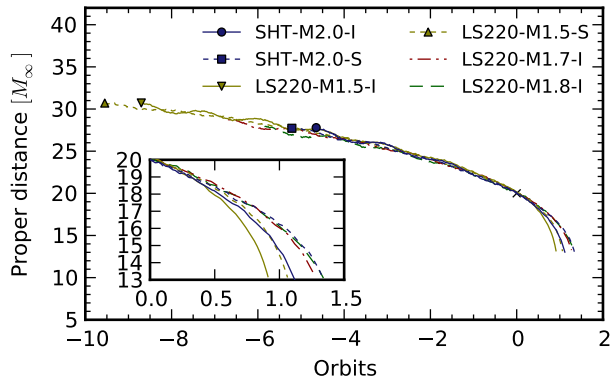


FIG. 3. Proper separation of maximum density locations versus their orbital phase. The phase has been aligned at a fixed separation of $d = 20 M_\infty$. The symbols are marking the start of the simulations.

simulations with otherwise identical setup, in particular starting at the same proper separation, we find that the spinning models require more orbits to reach a given separation. The influence of the spin grows stronger closer to the merger, as visible in the inset of Fig. 3. This “orbital hangup” has already been observed in our previous work [22] for models with an ideal gas EOS, as well as in [20, 21] using two different methods of adding the spin.

The main properties of the merger remnants are summarized in Table II. To quantify the HMNS lifetime, we define $\tau_{\text{HMNS}} = t_{\text{BH}} - t_{\text{m}}$, where t_{BH} is the (coordinate) time the apparent horizon first appears, and t_{m} is the time of the first maximum of the rest mass density after the stars touch. If the maximum density just increases until a BH is formed we call it a prompt collapse. The values reported for τ_{HMNS} should be taken with care, since HMNS lifetimes longer than a few ms are increasingly sensitive to numerical errors. However, we can reliably determine the minimum mass M_∞ required for prompt collapse, M_∞^{thr} . From Tables I and II, we obtain a value $M_\infty^{\text{thr}} = 1.5 M_\odot$ for the LS EOS, and $M_\infty^{\text{thr}} = 1.9 M_\odot$ for the SHT EOS, with an estimated error of $\pm 0.1 M_\odot$. This confirms in full GR the respective values reported in [7], which were obtained using the conformal flatness approximation.

We now discuss the spin of the final BH, $\chi_{\text{BH}} = J_{\text{BH}}/M_{\text{BH}}^2$, given in Table II. In Fig. 4, it is shown as a function of the additional NS spin, together with earlier results from [22] for an ideal gas EOS. Again, we find a slightly increased BH spin for the spinning model compared to the irrotational model. The absolute BH spin for models LS220-M1.5-I and -S (the ones resulting in a delayed collapse) is however significantly lower than for the other models, in particular the heavier ones with identical EOS. The disk remaining outside the BH on the other hand possesses $\approx 9\%$ of the BH angular momentum, while for the heavier models, mass and angular momentum of the disks are negligible. We conclude that the main reason for the lower BH spin is the angular momentum contained in the disk surrounding the HMNS.

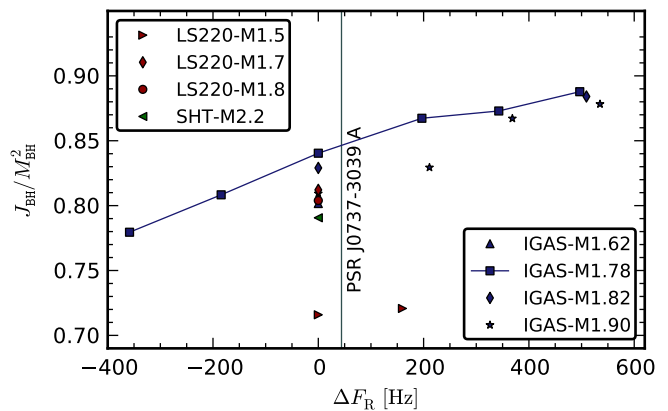


FIG. 4. Dimensionless BH spin versus initial NS spinup rate ΔF_R (see main text). Our results are shown in comparison to earlier results [22] for the case of an ideal gas EOS. The vertical line marks the rotation rate of the double pulsar PSR J0737-3039A.

Model	τ_{HMNS} [ms]	M_{BH} [M_\odot]	χ_{BH}	M_{D} [M_\odot]
SHT-M2.0-I	> 16.9	—	—	—
SHT-M2.0-S	> 9.4	—	—	—
SHT-M2.2-I	prompt	3.73	0.791	0.00
LS220-M1.5-I	8.6	2.65	0.716	0.06
LS220-M1.5-S	7.7	2.67	0.721	0.04
LS220-M1.7-I	prompt	2.98	0.812	0.00
LS220-M1.8-I	prompt	3.14	0.804	0.00
LS220-M1.4-U	> 29.8	—	—	—

TABLE II. Key properties of the mergers. τ_{HMNS} denotes the HMNS lifetime (see main text), unless the merger results in a prompt collapse to a BH. For models which did not collapse we report the post-merger duration of the simulation instead. M_{BH} is the final BH mass, $\chi_{\text{BH}} = J_{\text{BH}}/M_{\text{BH}}^2$ its dimensionless spin. The baryonic mass outside the BH at the end of each simulation is denoted by M_{D} .

B. Hypermassive neutron star properties

In this section we investigate the properties and dynamics of the HMNSs. For this purpose, we use the moments in the orbital plane defined by Eq. (4), with a cutoff radius $R = 30$ km that is sufficiently large to cover the oscillating HMNS. We recall that the construction of the coordinates used in the definition of the moments eliminates ambiguities due to the spatial gauge of the coordinates used in the simulation.

The most basic HMNS property is the size, which we quantify in terms of the density weighted average circumferential radius, i.e., $\bar{R}_c = P_0^{\rho r c}/P_0^\rho$. The time evolution of this measure is shown in Fig. 5, while the corresponding oscillation frequencies are reported in Table III. For the irrotational model SHT-M2.0-I, the star initially undergoes strong radial oscillations, which are however damped almost completely within 10 ms after the merger. The stellar radius \bar{R}_c

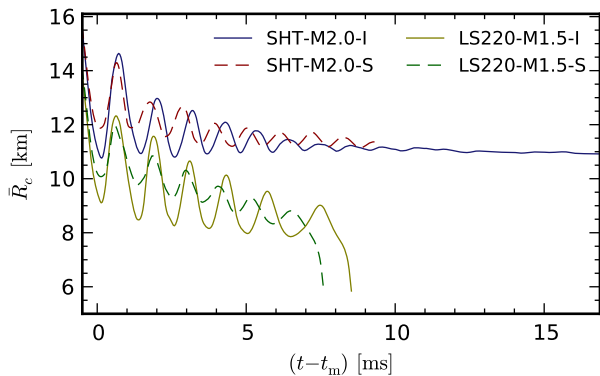


FIG. 5. Evolution of the HMNS average circumferential radius \bar{R}_c . The time coordinate is relative to the merger time t_m .

changes only very slightly after this point until the end of the simulation. Therefore, this model might remain stable considerably longer.

The evolution of \bar{R}_c for spinning model SHT-M2.0-S differs mainly in one respect from the irrotational case. As one can see in Fig. 5, the oscillation amplitude as well as the maximum compactness reached for the spinning case are smaller. The reason for this effect might be a larger centrifugal barrier due to the additional angular momentum. On the other hand, the compactness differs much less once the stars settle down. Equally likely, the difference may be caused by the slightly different impact trajectories, i.e., the orbital hangup discussed in Sec. IV A. The different oscillation amplitude will turn out to be important for the GW spectrum and for the ejection of matter, as we show below.

The HMNSs for models LS220-M1.5-I and -S, although less massive, are smaller than the SHT-M2.0 models. Their radii show a continuous drift in addition to the oscillations, until they collapse to a BH. When approaching the collapse, the frequency of the radial oscillation strongly decreases. This is to be expected, since the frequency of the (linear) quasi-radial mode also approaches zero for marginally stable models of isolated NSs. The radial frequency given in Table III in this case represents only an average value. We note that also for those models, the irrotational one becomes more compact than the spinning one during the initial oscillations.

Next, we study the rotation of the HMNSs. We define a density weighted average angular velocity in the orbital plane as $\bar{\Omega}_R = P_0^{\rho\Omega} / P_0^\rho$, where Ω is defined by Eq. (7). Fig. 6 depicts the evolution of the rotation rate. For all models, it shows a strong modulation, which turns out to be anti-correlated with the radius \bar{R}_c . This should be expected if angular momentum can be considered constant on the timescale of the oscillation period. Note that the radial oscillation frequency is similar to the rotation rate for models SHT-M2.0-I and -S, and even smaller for models LS220-M1.5-I and -S.

To quantify the amount of differential rotation, we use the ϕ -averaged rotation rate $\omega_R(r) = p_0^\Omega(r)$. We recall that rigid rotation implies that Ω , and hence ω_R , are constant. We com-

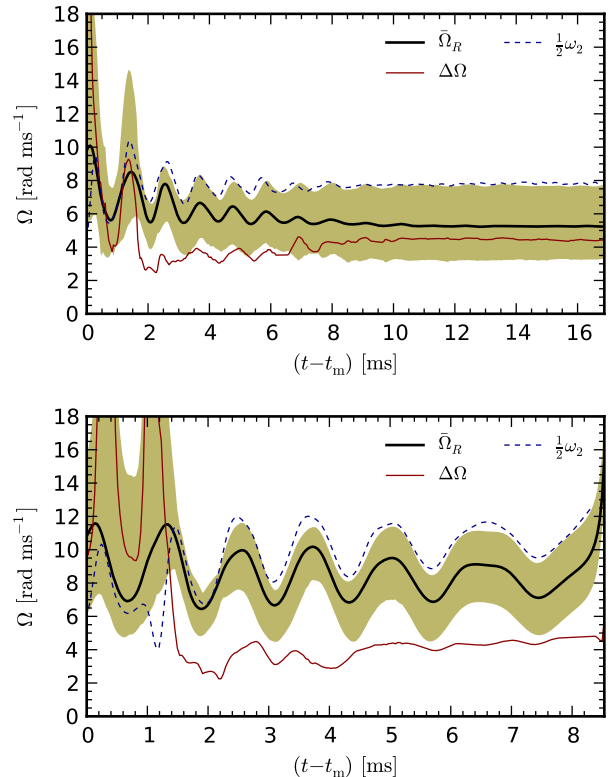


FIG. 6. Time evolution of the HMNS rotation for models SHT-M2.0-I (top panel), and LS220-M1.5-I (lower panel). The black solid line shows the average angular velocity $\bar{\Omega}_R$. The shaded area is bounded by the extrema of the angular velocity ω_R in the orbital plane inside the HMNS (ignoring mass densities below 10^{-2} of the maximum one). The difference $\Delta\Omega$ between maximum and minimum is given by the red curve. The dotted line shows the pattern angular velocity $\frac{1}{2}\omega_2$ of the $l = m = 2$ mode, computed from the phase velocity of P_2^p .

pute the extrema of ω_R within the HMNS at each time, shown in Fig. 6. The average values are reported in Table III. All our HMNSs possess a high degree of differential rotation, which fluctuates less than the rotation rate itself. Interestingly, it is slowly increasing. This has to be a consequence of the change in compactness, since dissipative effects can only decrease the differential rotation.

The rotation profile $\omega_R(r)$ reached after the stars have settled down is pictured in Fig. 7. In order to eliminate the modulation due to the oscillations, we construct an averaged neutron star (ANS in the following), averaging first in ϕ -direction and then in time. The time interval chosen for averaging is 5–9 ms after the merger for the SHT models, and 3–7 ms for the LS220 models. The rotation rate at the center is close to the minimum one, while the maximum appears in the outer layers of the star. This is true at all times, except during the merger phase, where the maximum rotation rate is reached in the central region. When comparing the spinning models to the irrotational ones, we find an increased average rotation rate, as one would expect. The maximum rotation rate of the spinning models on the other hand is similar or even smaller

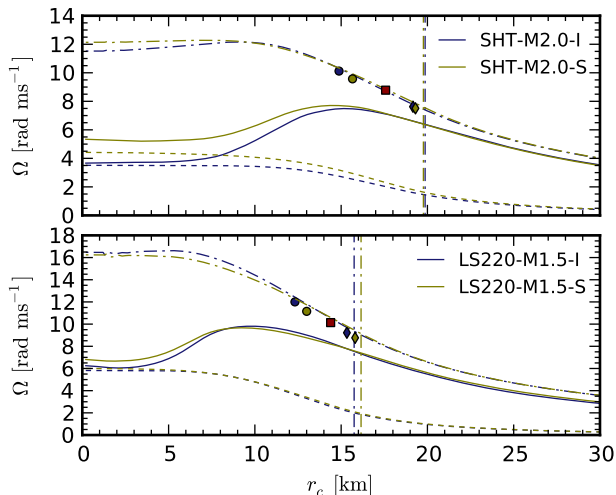


FIG. 7. Average rotation profile and Keplerian angular velocity profile for models SHT-M2.0-I and -S (top panel), and LS220-M1.5-I and -S (bottom panel). The solid curves mark the angular velocity ω_R in the orbital plane versus circumferential radius r_c . The dotted lines show the contribution $-\beta^\phi$ of the frame dragging. The dash-dotted curves are an estimate of the angular velocity of test particles in corotating circular orbits. The vertical dashdotted lines mark the radius where the mass density falls below 5% of the central one. For comparison, the circles mark radius and equatorial orbital velocity of cold, uniformly rotating stars with the same central rotation rate and central rest mass density. The diamonds mark models at zero-temperature with the same central rest mass density, uniformly rotating at Keplerian rate. The red squares mark the maximum mass (Keplerian) model for uniformly rotating cold NSs.

than for the irrotational models.

On a side note, the rotation as seen from infinity in the center of the ANSs is almost completely due to the frame dragging effect, i.e., the fluid is rotating slowly with respect to the local inertial frame. This is visualized in Fig. 7, which also contains the frame dragging contribution $-\beta^\phi$ to the rotation rate Ω , see Eq. (7).

Armed with the rotation profile, we will now investigate why the system does not immediately collapse to a BH despite the total baryonic mass exceeding the maximum one for a cold, uniformly rotating star in β -equilibrium. There are two possibilities: thermal effects and differential rotation. As pointed out in [49], increasing the (uniform) temperature tends to decrease the maximum mass of stars rotating uniformly or differentially with a j -constant law. In [27], the same was found for non-rotating stars with constant specific entropy. Further, we find that the maximum baryonic mass of uniformly rotating stars obeying the LS220 EOS with constant specific entropy of $4 k_B$ (and β -equilibrium) is reduced by 15% compared to the zero-temperature case. Although the situation for differential rotation may be different, it seems unlikely that temperature is responsible for stabilizing the merger remnants produced in our simulations.

We are left with differential rotation to support larger masses than the maximally but uniformly rotating models.

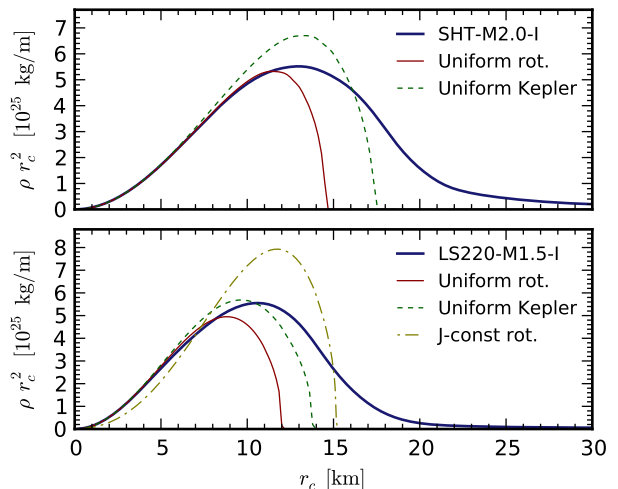


FIG. 8. Density profile in the equatorial plane of the time and ϕ -averaged HMNS for models SHT-M2.0-I (top panel), and LS220-M1.5-I (bottom panel). For comparison, we show the density profiles of uniformly rotating NS stars with same central density and central rotation rate as the HMNS, and same central density but maximum rotation rate. For the LS220 case, we also show a model with same mass as the HMNS, but a j -const rotation law (see main text). The density is scaled by r_c^2 to better visualize the contribution of each spherical shell to the total mass. Note however that since the models are not spherically symmetric, simply taking the integrals of the curves would overestimate the total mass inside a given radius.

Model	$F_{\text{Rot}}^{\text{min}}$ [kHz]	$F_{\text{Rot}}^{\text{max}}$ [kHz]	F_{Rad} [kHz]	F_2^2 [kHz]
SHT-M2.0-I	0.66	1.20	0.94	2.47
SHT-M2.0-S	0.85	1.45	0.95	2.66
LS220-M1.5-I	0.96	1.56	0.76	3.24
LS220-M1.5-S	1.05	1.62	0.89	3.17
LS220-M1.4-U	n.a.	n.a.	1.45	2.93

TABLE III. HMNS frequencies. The minimum and maximum rotation rates inside the HMNS are denoted $F_{\text{Rot}}^{\text{min}}$ and $F_{\text{Rot}}^{\text{max}}$, respectively. The values are time averages over the interval starting 2 ms after the merger until the end of the simulation or the collapse to a BH. The radial oscillation frequency F_{Rad} was computed from the Fourier spectrum of \bar{R}_c . The average frequency F_2^2 of the $l = m = 2$ oscillation mode was extracted from GW effective strain spectrum.

This has been discussed mainly for rotation laws where the core rotates faster than the outer layers, see [12, 49]. However, this picture does not apply to the remnants formed in our simulations. We computed the stellar models with the same central rest mass density as the ANS, but rotating uniformly at the Kepler limit, as well as the maximum mass Kepler model. Radius and rotation rate are compared to the ANS rotation profile in Fig. 7. As one can see, the rotation rate of the ANS core is significantly lower. The notion that a dense core rotating more rapidly than the Keplerian model is responsible for stabilizing the mass against collapse is thus ruled out for the equal-mass models presented here (but not in general). Note a

similar rotation profile has also been reported in Fig. 8 of [24] for different models. Besides the rotation rate, the central density of the ANS is also lower than the one of the Keplerian maximum mass model, around 75% and 83% for the for the SHT and LS220 EOS models, respectively.

As pointed out in [12], another option to increase the maximum mass is the addition of an extended Keplerian disk. Even if the rotation profile is only close to the Keplerian one, it should be possible to create a massive envelope. Indeed, we find that the density profile of our HMNS extends to larger radii than the ones of uniformly rotating stars. As shown in Fig. 8, the density profiles of uniformly rotating stars with same central density agree well in the core region, but the HMNS extends well beyond the surface of the uniformly rotating stars. For comparison, the baryonic masses of the uniformly rotating models with same central density and same central rotation rate (maximum rotation rate) are $2.46 M_\odot$ ($2.78 M_\odot$) and $3.12 M_\odot$ ($3.74 M_\odot$) for the LS220 and SHT models, respectively. This is 7 – 22% lighter than the total masses in our simulations (compare Table I). Figure 8 seems to indicate that the mass in the core regions of the HMNSs, up to ≈ 8 km for the LS220 models and ≈ 12 km for the SHT models, is similar to the uniform models, while supporting more mass further out. Note however that the density profile in the equatorial plane can only provide a very rough estimate for total mass in a given radius, due to the deviation from spherical symmetry. For lack of saved 3D data, we could not compare the exact mass-inside-radius relations.

Without doubt, there is a significant amount of mass in the extended outer layers. It is therefore natural to ask how close to Keplerian velocity our profiles are at a given radius. To obtain an estimate, we approximate the spacetime as stationary and axisymmetric with respect to the coordinates introduced in Sec. II C. We compute the metric components in the orbital plane using the same averaging as for the ANS rotation profile. The angular velocity Ω_K of test particles in a corotating circular orbit at each radius is then given by the larger solution of the quadratic equation

$$0 = g_{tt,r} + 2g_{t\phi,r}\Omega_K + g_{\phi\phi,r}\Omega_K^2. \quad (9)$$

The result, shown in Fig. 7, is that the ANSs have a large envelope moving shortly below Keplerian velocity. However, it is difficult to estimate the error of the Keplerian velocity profile due to the non-stationarity of the actual spacetime. As a cross-check, we also compare with the equatorial orbital velocity of uniformly rotating models with the same central density and rotation rate as the ANSs (circles in Fig. 7). Assuming that the orbital velocities are mainly determined by the dense core, this provides us with a rough, but independent estimate. As shown in Fig. 7, it matches the first one surprisingly well. Curiously, also the maximum mass Kepler models (red squares in Fig. 7) are located very close to the Kepler profile of the simulation results.

We note that the rotation profile is only an average of a very dynamic system, in particular for the LS220 models, which also undergo a drift to higher compactness in addition to the large oscillations. That said, *the above findings strongly suggest that the system is stabilized against immediate collapse*

by an extended, almost-Keplerian envelope. We consider this to be the important aspect of the rotation profile with respect to stabilizing the mass, not the slow rotation of the core. For the irrotational LS220 model, we checked that it is also possible to construct a HMNS with the same mass but a j -const rotation law. The model we constructed is shown in Fig. 8. It has a central rotation rate of $\Omega_c = 1.694$ kHz and a differential rotation parameter $A = 1.48$ km. In contrast to the other models, the density maximum is not at the center due to the rapid core rotation.

We now turn our attention to the non-axisymmetric perturbations of the HMNS. The amplitudes of the density moments P_m^ρ are plotted in Fig. 9. We first discuss the $m = 2$ component, which is clearly dominant. Obviously, it is excited by the merger and then slowly decays. In order to interpret the meaning of $P_2^\rho(t)$, we also studied the phase of $p_2^\rho(t, r)$. We found that during the plunge, the phase of p_2^ρ naturally follows the average orbital phase of the two stellar cores. During the subsequent merger stage the phase varies strongly inside the forming HMNS. This could be caused by the presence of several oscillations of comparable strength. However, we feel that this stage is genuine nonlinear and do not interpret it in terms of perturbation theory. 1–2 ms after the merger time t_m however, the $m = 2$ perturbation becomes dominated by a single oscillation mode, i.e., the phase of p_2^ρ is independent of the radius. Only in the outer layers of the star, at densities around 5% of the central one, the oscillations are out of phase. Considering the large oscillation amplitude, this is quite normal. As discussed in [50], the nonlinear effects at the surface will contribute to the damping of the mode, probably more than gravitational radiation.

Since during the HMNS stage there exists one strongly dominant $m = 2$ oscillation mode, the phase velocity of P_2^ρ is a good estimate for its instantaneous oscillation frequency ω_2 . In Fig. 6, ω_2 is shown in comparison to the rotation rates. Note the value is only meaningful once P_2^ρ is dominated by the $m = 2$ oscillation mode, which happens after ≈ 2 ms. As one can see, *the frequency is strongly modulated. This has to be taken into account when interpreting the Fourier spectra of GW signals*, as will be discussed in Sec. IV C. Clearly, the frequency is also strongly correlated with the rotation rate. A heuristic explanation can be obtained by regarding the radially oscillating HMNS as a sequence of fixed background models for the $m = 2$ mode oscillation, which has a higher frequency. For uniformly rotating stars, it is known that the frequency in the corotating frame depends weakly on rotation rate. The frequency of the corotating mode in the inertial frame is shifted by $+m\Omega$. The resulting estimate $\delta\omega_2 \approx 2\delta\Omega$ fits our data remarkably well.

Let us now return to the remaining moments P_m^ρ shown in Fig. 9. For all HMNSs, we observe the growth of $m = 1$ and $m = 3$ components. For the SHT-M2.0-I model, the $m = 1$ perturbation becomes as large as the main $m = 2$ mode at the end of the simulation. For the LS220-M1.5 models, the HMNS starts collapsing before this happens. During the collapse, the $m = 1$ moment is rapidly amplified. We did not identify the exact nature of those components, but similar results have been reported in [21] for BNS mergers of spinning

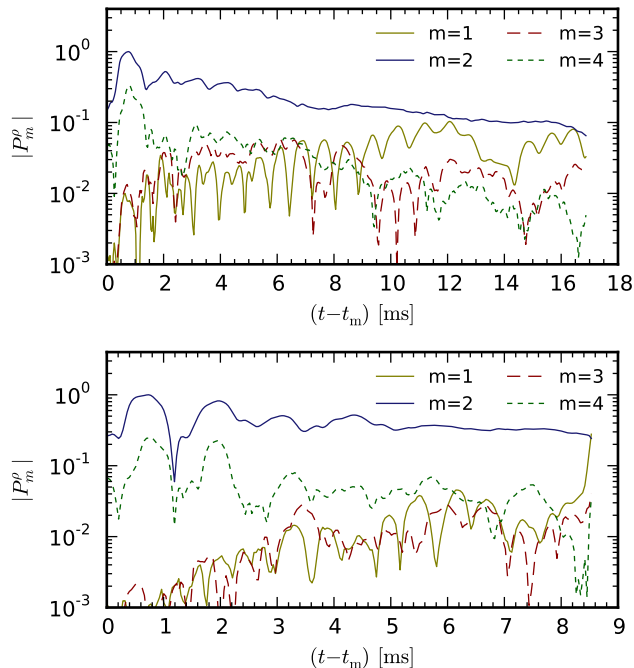


FIG. 9. Time evolution of the density moment amplitudes $|P_m^\rho|$ for models SHT-M2.0-I (top panel) and LS220-M1.5-I (bottom panel). The amplitudes are normalized to the maximum of the $m = 2$ moment.

stars employing an ideal gas EOSs. Lastly, the $m = 4$ pattern possesses the same angular velocity as the $m = 2$ mode, and both moments are, on average, decaying. We therefore attribute the $m = 4$ moment to the non-harmonic ϕ -dependency of the $m = 2$ oscillation mode, which in turn is due to the large amplitude.

A rather surprising result is that the angular velocity $\dot{\phi} = \frac{1}{2}\omega_2$ of the $m = 2$ mode pattern is almost equal to the maximum angular velocity of the fluid for all equal-mass models, as one can see in Fig. 7. There are two likely explanations besides pure coincidence. Either the mode frequency is somehow determined by the maximum angular velocity for our models, or the oscillation of the bulk affects the rotation rate of the outer layers. Animations of our simulations reveal strong nonlinear effects close to the surface, such as mass shedding. On the other hand, this does not explain why the rotation rate decreases again toward the surface. In any case, this relation deserves further scrutiny in future studies.

C. Gravitational waves

In the following we will discuss the features of the gravitational wave signal extracted from our simulations. The focus will be on relating the GW spectra to the dynamics of the HMNSs. For simplicity, we did not extrapolate the signals to infinity, but use a finite extraction radius of 756 km and 916 km for the LS220 and SHT models, respectively.

We begin with the equal mass models. In all cases, the GW

strain multipole moments are dominated by the $l = m = 2$ term, followed by the $l = 2, m = 0$ contribution, which has a maximum strain around 6–8% of the former. The $m = 3$ perturbation which develops for the HMNSs (see Sec. IV B) is also visible in the $l = m = 3$ moment of the respective GW signals, but the amplitude just amounts to 1–2% of the dominant mode. The GW strain of the $l = m = 2$ contribution is shown in Figs. 10 and 11. When comparing the spinning models to the nonspinning ones, differences in the GW signal are visible by eye. Besides the orbital hangup during the inspiral, the modulation during the HMNS phase is different. We will come back to this issue later.

First, we try to understand the GW spectrum. As discussed in Sec. IV B, the oscillation frequency of the main $l = m = 2$ oscillation mode is strongly modulated due to the radial oscillation. This will at least broaden the corresponding peak in the Fourier spectrum. Considering that the signal spends more time in a given frequency bin near a local extrema of the modulated frequency, one might expect the appearance of additional side peaks located in proximity to the extrema. To explore the effects of frequency modulation on the Fourier spectra, we synthesize a toy model signal given by

$$z = e^{i\phi(t) - \frac{t}{\tau_s}} \quad (10)$$

$$\phi(t) = 2\pi f_s t - \frac{\Delta f}{f_m} \cos(2\pi f_m t) e^{-\frac{t}{\tau_m}} \quad (11)$$

This corresponds to a signal with a sinusoidal frequency modulation, where both the signal and the frequency modulation amplitude decay exponentially, on different timescales. Figure 12 shows the instantaneous frequency $\dot{\phi}$ and the Fourier spectrum of z , where we chose parameters approximating real signals. Indeed, we observe several peaks in the spectrum which are located near local extrema of the instantaneous frequency. We stress that this is not an exact relation, and not all local extrema cause separate peaks. Further, we even find a peak at a frequency larger than the maximum instantaneous frequency, although it is rather small. Note the appearance of additional peaks due to frequency modulation is an entirely different effect than the so called combination frequencies, i.e., side peaks arising in Fourier analysis of monochromatic signals superposed in a non-linear fashion. We expect both effects in our results.

The effective strain spectrum for the two irrotational models forming a HMNS is given in the upper panels of Figs. 13 and 14. In order to distinguish peaks that can be attributed to oscillations of the HMNS from peaks caused by the plunge and merger stage, we also show the spectrum of the late signal, starting 2 ms after the time of the first density maximum during the merger. The comparison shows that the dominant peak f_2 clearly originates from the HMNS phase in all cases. The low frequency peak f_1 on the other hand is strongly suppressed in the late signal, and therefore has to be caused by the plunge and merger. More precisely, it seems to originate from the times of the plunge and the maximal expansion after the first 1–2 bounces. At this time the system still resembles more two separate cores in an eccentric orbit inside a common envelope than a deformed single star (compare Fig. 1). We note that in [2], the low frequency peak (for different models) has

been attributed to a combination frequency of the quasi-radial and $m = 2$ mode oscillation of the HMNS. For the cases at hand, this interpretation does not apply. To distinguish between the two causes of the low frequency peak, one has to study the late GW signal separately.

To interpret the remaining peaks, we need to take into account the modulation of the $l = m = 2$ mode frequency. For this, we juxtapose the instantaneous frequency of the $l = m = 2$ component of Ψ_4 to the Fourier spectra in Figs. 13 and 14. The largest peak f_2 clearly corresponds to the average instantaneous frequency. Moreover, sidepeak f_4 in Fig. 14 is located at the same frequency as two of the minima of the instantaneous frequency. It is thus plausible that this peak is caused by the very same oscillation mode as peak f_2 .

The high-frequency peak f_3 is located shortly below the global maximum of the instantaneous frequency, similar to what we found for the synthetic signal discussed earlier. The maximum frequency is reached during the merger when the star is most compact. For model LS220-M1.5-I, the maximum frequency is reached again during the second bounce. For both models however, the distance of peak f_3 to the main peak *also* agrees with the mean radial oscillation frequency (see Table III). For model SHT-M2.0-I, peak f_3 is barely visible in the spectrum of the late signal and should therefore be attributed to the merger phase instead to a combination frequency. For model LS220-M1.5-I on the other hand, peak f_3 is still present in the late signal, although smaller. Therefore it is most likely an overlap of the $l = m = 2$ oscillation itself at the time of maximum compactness, and a combination frequency of the same mode at the HMNS stage with the radial oscillation frequency. The agreement of those frequencies is most likely a coincidence. The shift of the maximum of the $l = m = 2$ mode frequency relative to the central value depends on the amplitude of the radial oscillation during the merger, while the shift of the combination frequency is given by the frequency of the radial mode.

Our findings indicate that one cannot securely associate such high frequency peaks either to the merger stage, a combination frequency, or even a separate HMNS oscillation mode. For this, one needs to consider the late part of the spectrum separately. Of course, this requires a high signal-to-noise ratio. We stress that the merger phase does not necessarily leave a strong imprint in the GW signal. Figure 15 shows the GW spectrum and instantaneous frequency evolution for the unequal mass model LS220-M1.4-U. As one can see, there is no significant high frequency peak at all. Also, the only low frequency peak is very broad and of low amplitude. It seems to originate simply from the final part of the inspiral.

In order to link the GW signal to the dynamics of the HMNS, we also included the spectrum and instantaneous frequency of the fluid moment P_2^o in Figures 13 and 14. The frequencies of the three main peaks agree well with the GW signal. Note the moments use a different radial weight than one would use in the quadrupole formula to estimate the GW strength. This might explain the different amplitude of the low frequency peak. Also, since the fluid mode phase velocity depends on the radial weight unless there is only one dominant oscillation mode, the differences to the GW phase velocity

during the merger stage are to be expected. Finally, the inspiral part is missing in the spectrum of P_2^o because we only start computing it shortly before the merger.

We now return to the influence of the spin on the waveform. The spectra and instantaneous frequencies of spinning and irrotational models are compared in Figures 16 and 17 for the models with SHT and LS220 EOS, respectively. Note that for cases where the HMNS does not collapse, the exact shape of the GW spectrum depends on the evolution time. A longer simulation enhances the contribution from the monochromatic late signal. In order to avoid such selection effects when comparing spinning and non-spinning GW spectra, we cut the GW signal from the longer simulation such that the duration after the merger matches the shorter simulation. The relative peak amplitudes in Figs. 13 and 16 are indeed different.

The frequency shift of the main peak for the spinning models with respect to the irrotational ones is smaller than the width of the peak. The main difference between the two cases is that the maximum instantaneous frequency reached during the merger is slightly smaller for the spinning models, which in turn is related to the weaker radial oscillation (see Sec. IV B). Peaks which represent combination frequencies with the radial mode should thus have smaller amplitudes, while peaks representing the maximum frequency during the merger should be located at slightly lower frequency. Indeed, peak f_3 is split into two smaller peaks for the spinning LS and SHT EOS models, which further substantiates our interpretation. Unfortunately, *the dependency of the GW spectrum on the spin is a complicated one, and it would be extremely difficult to infer the spin from spectra* like the ones presented here.

D. Matter ejection

Finally, we study the mechanisms leading to the ejection of matter during and after the merger, in particular the amount of unbound matter. The models undergoing prompt collapse have no significant disk and no unbound matter. Hence we only discuss the ones producing a HMNS.

A significant amount of matter is ejected from the remnant during the merger, but also at later stages. A large part of the matter ejected during the merger forms an envelope/disk which does not become unbound. The main effect leading to unbound matter for our equal-mass models seems to be shock formation. The $m = 2$ mode oscillation is highly nonlinear at low densities, causing two spiral shaped shock waves, which in turn liberate matter from the disk. Effects like this have also been observed by [9] for various equal-mass models with hybrid EOSs. The shape of the expanding shock fronts in the orbital and xz -planes is illustrated in Fig. 18. Moreover, the strong radial oscillation modulates the strength of shock formation, such that each wave of ejected matter can be traced back to a radial oscillation (or the merger itself). The evolution close to the NS is pictured in Fig. 19, displaying a spacetime diagram of the ϕ -averaged temperature in the orbital plane. Outside a radius ≈ 15 km, one can easily spot outgoing waves of increased temperature. The comparison

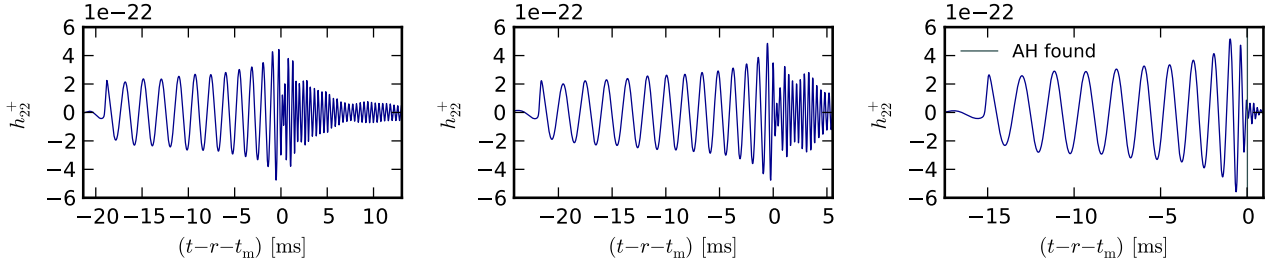


FIG. 10. Gravitational wave strain at distance 100 Mpc for models SHT-M2.0-I (left panel), SHT-M2.0-S (middle panel), and SHT-M2.2-I (right panel). The waveforms were extracted at radius $r = 916$ km.

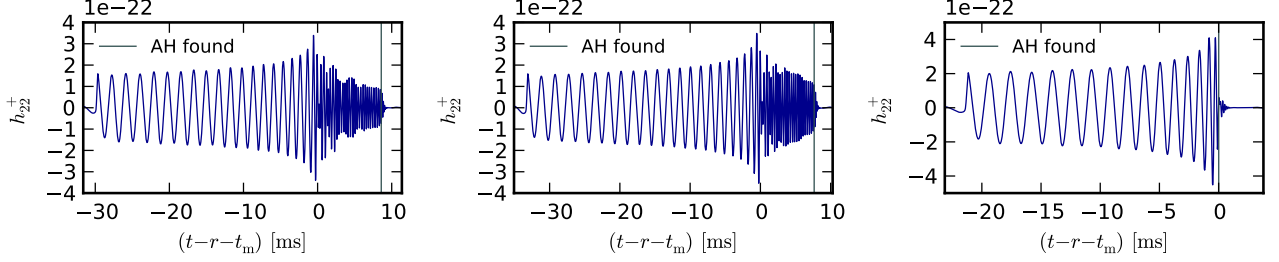


FIG. 11. Gravitational wave strain at distance 100 Mpc for models LS220-M1.5-I (left panel), LS220-M1.5-S (middle panel), and LS220-M1.8-I (right panel). The waveforms were extracted at radius $r = 756$ km.

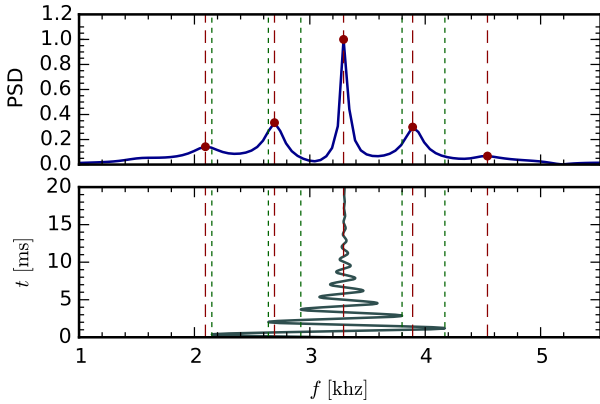


FIG. 12. (Top panel) Fourier spectrum of toy signal, with values $f_s = 3.3$ kHz, $\Delta f = 1.3$ kHz, $\tau_s = 8$ ms, $\tau_m = 3$ ms, $f_m = 0.6$ kHz. (Bottom panel) Corresponding instantaneous frequency. The vertical dashed lines mark the maxima of the Fourier spectrum, the vertical dotted lines the first five extrema of the instantaneous frequency.

with the average radius (marked by the green line) reveals that they are clearly correlated with the radial oscillation.

In order to compute the amount of matter that will escape to infinity, we integrate the density of unbound matter over the whole computational domain. There are two options for estimating whether or not a fluid element is bound. Both assume a stationary spacetime and coordinates such that t^μ is a Killing vector. The first criterion, which is also used in [9], is based on the assumption that fluid elements move along geodesics. This implies that the 4-velocity u^μ satisfies $u_t = \text{const.}$ At

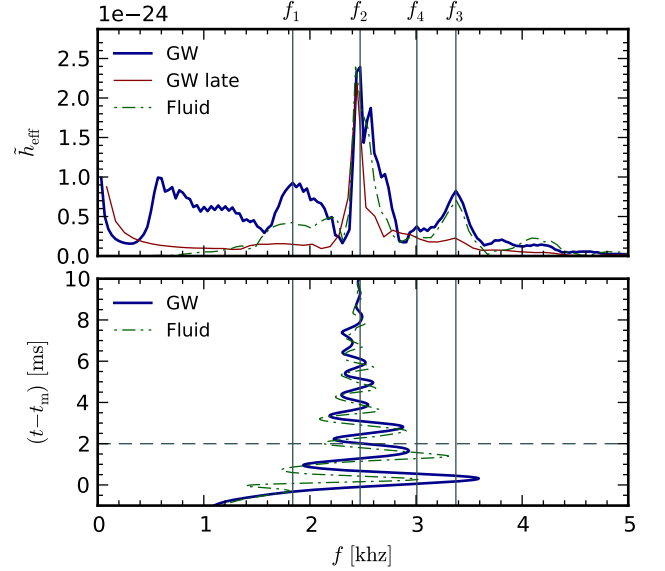


FIG. 13. (Top panel) GW effective strain spectrum for model SHT-M2.0-I. The thick blue curve shows the spectrum of the full signal at a nominal distance of 100 Mpc. The red solid line shows the spectrum of the late signal, starting 2 ms (plus time of flight) after the time of the first density maximum during the merger, t_m . The green dash-dotted line depicts $f^2 \tilde{P}_2^p(f)$, where \tilde{P}_2^p is the Fourier spectrum of the fluid moment P_2^p , rescaled to match the maximum amplitude. (Bottom panel) Evolution of the instantaneous frequencies of the GW signal Ψ_4 (thick blue line), and the moment P_2^p (green dash-dotted line). The GW signal has been shifted to compensate for the time of flight.

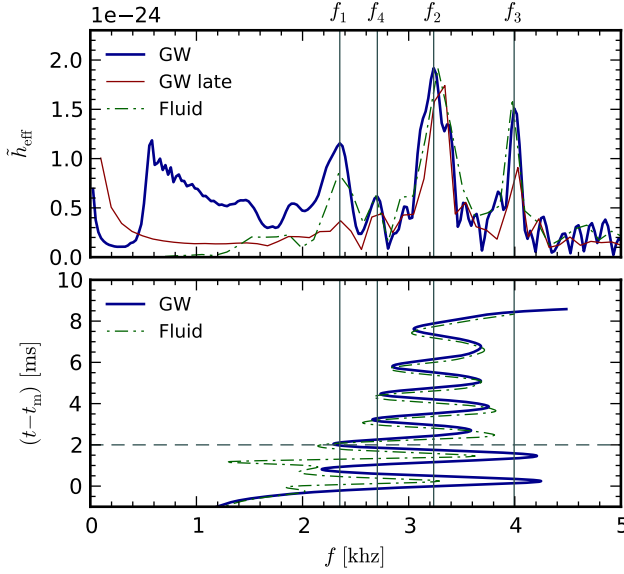


FIG. 14. Like Fig. 13, but showing model LS220-M1.5-I.

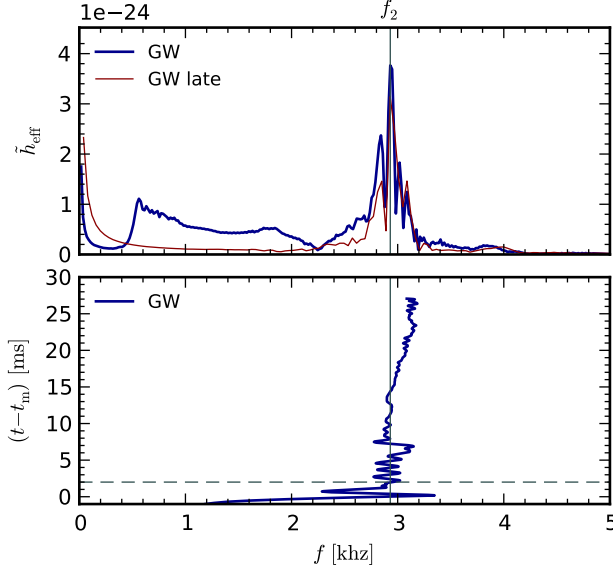


FIG. 15. Like Fig. 13, but for unequal-mass model LS220-M1.4-U.

infinity, $u_t = -W$, where W is the Lorentz factor. A fluid element would hence be able to reach infinity if $-u_t > 1$, approaching an escape velocity of $v_e^2 = 1 - u_t^{-2}$. This criterion is only meaningful if the pressure forces stay small compared to the gravitational ones. In the context of NS mergers, this is not the case near the remnant. Pressure forces mainly accelerate material outwards, such that it may become unbound at a later time. The geodesic criterion tends to underestimate the amount of unbound matter. We use it to obtain a lower limit.

The second option is to assume a stationary relativistic fluid flow, for which hu_t is conserved along fluid worldlines. We note that the relativistic enthalpy h is only defined up to a

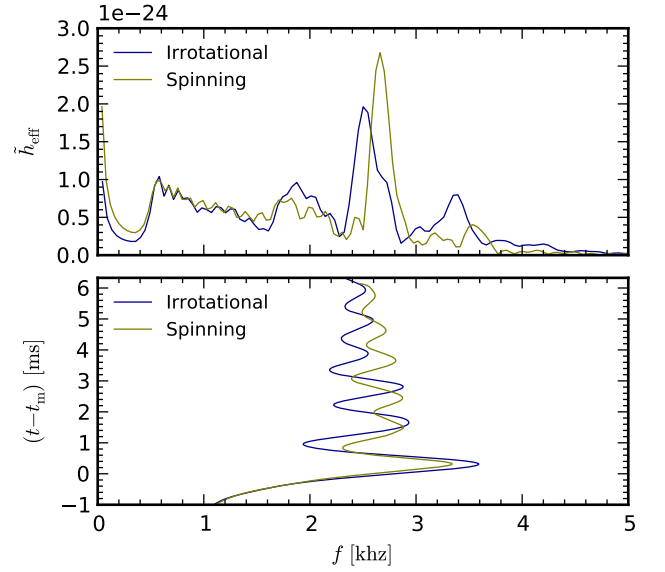


FIG. 16. (Top panel) GW effective strain spectrum at nominal distance of 100 Mpc for irrotational model SHT-M2.0-I compared to the same spectrum for spinning model SHT-M2.0-S. The GW signal from the longer simulation was cut such that the signal duration after the merger matches the shorter simulation. (Bottom panel) Evolution of the corresponding instantaneous frequencies.

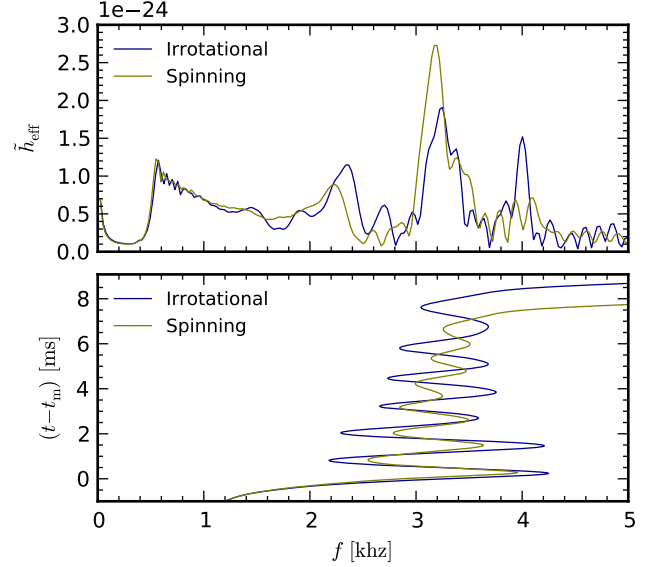


FIG. 17. Like Fig. 16, but for models LS220-M1.5-I and -S.

constant factor that depends on the formal baryon mass used to define the rest mass density ρ in terms of the baryon number density. In our simulations, we chose this constant such that $h \rightarrow 1$ when density and temperature tend to zero. We then assume that this limit is approached by the fluid at infinity, and arrive at the Bernoulli criterion $-hu_t > 1$. The Bernoulli criterion might overestimate the role of internal energy for liberating matter. In our simulations, shock formation is an im-

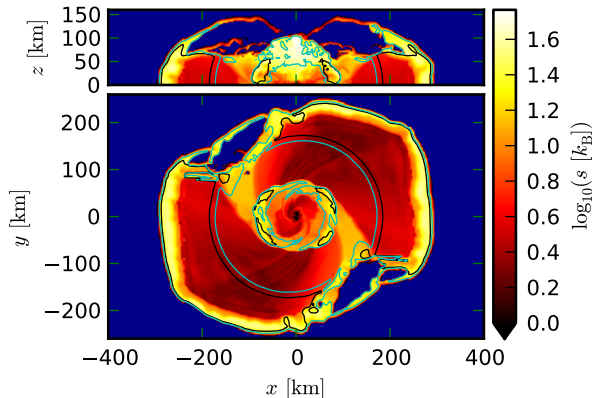


FIG. 18. Specific entropy in the orbital plane, 2.5 ms after the merger, for model SHT-M2.0-I. The regions where matter is unbound according to the geodesic criterion are bounded by the black lines, the cyan lines enclose regions unbound according to the Bernoulli criterion. Regions covered by the artificial atmosphere are colored blue.

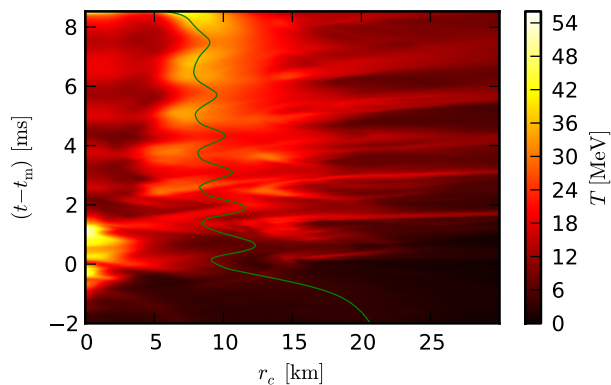


FIG. 19. Thermal evolution of model LS220-M1.5-I from merger until BH formation. The color corresponds to the ϕ -averaged temperature in the orbital plane as a function of circumferential radius and coordinate time. The green line marks the density averaged circumferential radius \bar{R}_c .

portant cause for matter ejection. The corresponding shock heating can increase the value of h , such that the Bernoulli criterion is satisfied. However, the assumption of a stationary fluid flow is a decidedly bad approximation near those shocks. In any case, the Bernoulli criterion generally predicts more unbound mass than the geodesic criterion. We note there is a third estimate used in [8, 51]. Contrary to [51], it is not the geodesic criterion, but in general closer to the Bernoulli criterion. It can be reformulated as $-hu_t > 1 + \frac{\alpha P}{W_p}$, where α is the lapse function.

A comparison between the Bernoulli and geodesic criteria is shown in Fig. 18. They agree well for the fluid in first wave of ejected material, which at this point is already very diluted. Closer to the remnant however, where the density is also higher, one can spot large differences near the

spiral shocks. Based on the data in the orbital plane at the time shown in Fig. 18, we estimate that the Bernoulli criterion yields at least two times more unbound matter than the geodesic one for model SHT-M2.0-I. For the unequal-mass model LS220-M1.4-U, we even find a ratio larger than five. In principle, the ratio could become arbitrary high in cases where the material is just marginally unbound according to the geodesic criterion. Also note the comparison in the orbital plane might not be representative for the full volume.

Another source of uncertainty is that the fluid is set to the artificial atmosphere wherever the density drops below $6 \times 10^7 \text{ g/cm}^3$ (close to the lowest tabulated density of the SHT EOS). At the time shown in Fig. 18, the first wave of ejected matter already exhibits patches covered by artificial atmosphere. Clearly, it would have been beneficial to use a lower density for the artificial atmosphere, extending the EOS if necessary. Another possible improvement for future simulations would be to use the time integral of the unbound matter flux through a sphere with a radius sufficiently large to avoid using criteria for boundness in highly dynamic regions.

Despite the above uncertainties, we can use the geodesic criterion to get a lower limit on the unbound mass. The time evolution of the formally unbound mass is shown in Fig. 20. Note that although the steepest increase occurs shortly after the merger, matter becomes unbound continuously, driven by the shock waves caused by the NS oscillations. The decrease at late times is a numerical artifact caused by matter diluted to artificial atmosphere density. We use the maximum as a lower limit for the total amount of matter that would escape to infinity. In addition, we evaluate the density-weighted average specific entropy and electron fraction, as well as the maximum escape velocity at the time this maximum occurs. The results are reported in Table IV. Note however that the electron fraction is passively advected and would in reality be changed by neutrino radiation of the hot and optically thin fluid. Model SHT-M2.0-I is also investigated in [8], using the conformal flatness approximation. They report an ejected mass of $9.08 \times 10^{-3} M_\odot$, which is compatible with our lower limit. Surprisingly, the amount of unbound matter for the spinning models is markedly smaller compared to the irrotational ones. We attribute this to the different amplitude of the radial oscillations shown in Fig. 5. *At least for equal-mass models, the initial NS spin can have a strong influence on the amount of matter ejected to infinity.*

V. SUMMARY AND DISCUSSION

In this work we have investigated in detail the merger and post-merger dynamics of irrotational equal-mass BNS models in comparison to models with initial NS spins aligned to the orbital angular momentum. The rotation rates considered are more than four times lower than the fastest observed pulsar, but still larger than any observed pulsar in a BNS system.

We have found that the spin affects the amplitude of the post-merger radial oscillations. The reason might be a slower impact due to the orbital hangup effect described in [20, 21], which we observe as well during the inspiral. The additional

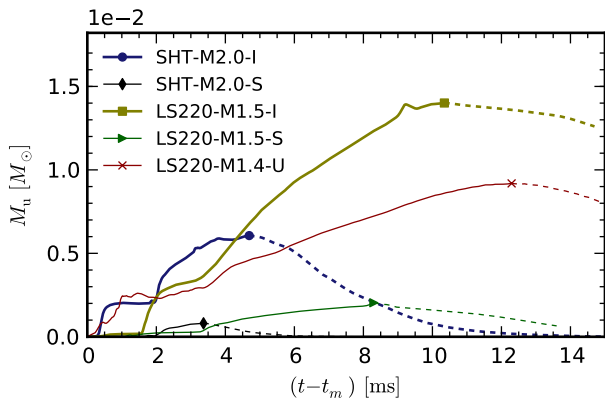


FIG. 20. Time evolution of the estimate for the mass of unbound matter, according to the geodesic criterion. The decreasing parts (dotted lines) are unphysical artifacts caused by the artificial atmosphere, the maximum serves as a lower bound for the real value.

Model	$M_u [0.01 M_\odot]$	$\bar{s} [k_B]$	\bar{Y}_e	v_e
SHT-M2.0-I	0.61	18	0.11	0.33
SHT-M2.0-S	0.08	23	0.10	0.44
LS220-M1.5-I	1.40	21	0.14	0.28
LS220-M1.5-S	0.20	18	0.09	0.24
LS220-M1.4-U	0.92	16	0.10	0.19

TABLE IV. Properties of unbound matter. M_u is the lower limit for the unbound mass, obtained from the maximum amount of unbound matter according to the geodesic criterion. At the time the maximum occurs, we compute the density weighted average of specific entropy and electron fraction, denoted by \bar{s} and \bar{Y}_e . v_e is the maximum velocity unbound material would reach at infinity.

angular momentum might also contribute by increasing the centrifugal barrier. The radial oscillation is noteworthy because it turns out to affect the GW spectrum as well as the amount of unbound matter.

The GW spectrum is affected by the radial oscillation because it leads to a modulation of the rotation rate. Furthermore, the main $m = 2$ oscillation mode frequency in the inertial frame is correlated with the rotation rate, and hence shows variations as well. The modulation of the frequency can become strong enough to create additional peaks in the GW spectrum. In particular, the frequency maximum reached when the star is most compact during the merger leads to a separate high-frequency peak for the equal-mass systems we studied. We also observed that local extrema of the instantaneous mode frequency can cause additional side peaks of the dominant peak. The frequency modulation and its influence on the GW spectrum was already described in [10]. In addition, we found the quantitative relation $2\Delta F_R \approx \Delta F_2$ between the modulation amplitudes of the average rotation rate and the $m = 2$ mode frequency. It is yet unknown if this relation holds in general.

The direct influence of the spin on the frequency of the $m = 2$ oscillation is weak for our models, comparable to the

width of the corresponding peak. Inferring the spin from the GW signal will prove difficult. On the other hand, a weak dependency on spin is advantageous when using the GW spectral features to break the mass-redshift degeneracy of the inspiral GW signal, as proposed in [52].

The appearance of additional peaks due to frequency modulation should not be confused with the so called combination frequencies, which can be present simultaneously. Indeed, we observed that the peak due to the maximum frequency of the main $m = 2$ mode reached during merger can overlap with a combination frequency between the post-merger $m = 2$ and radial modes. The low-frequency peaks on the other hand are dominated by the contribution from the plunge and the first one or two bounces for our models. At those phases, the system still exhibits a double core structure, which suggests that it might be better described in terms of orbiting cores with very strong tidal effects instead of interpreting it as one strongly oscillating star. This view is also supported by the discovery of EOS independent empirical relations for the low frequency GW signal from the merger phase, see [11, 53].

We stress that the above findings obtained for our selected models, which are all very massive, are not to be generalized. For example, the unequal-mass model we evolved shows only small modulation and no significant high- or low-frequency peaks. A large number of BNS mergers has been investigated in [10]. Some of those models led to a large modulation similar to the ones found in our simulations, while others showed a weak modulation (or drift), resulting only in the broadening of the main peak. Nevertheless, a consequence for GW analysis is that one needs to study the spectrum of the late signal separately in order to determine the nature of the high-frequency peaks. The interpretation as combination frequencies proposed in [2] does not hold in general.

Another important aspect of the merger, besides the GW signal, is the amount, composition, and temperature of the matter ejected from the system. For our models, matter is liberated in several waves along spiral shock waves originating from the HMNS. The first wave is launched during the merger itself. The subsequent high-amplitude $m = 2$ oscillation causes a shock wave in the form of a double spiral. The initial strength is modulated by the radial oscillation. We observe that more material becomes unbound for the irrotational models, which is most likely due to the stronger radial oscillations we observe for this case.

One of our irrotational models was also evolved by [8]. Their estimate for the amount of ejected matter, which is based on a prescription similar to the Bernoulli criterion, is compatible with our lower limit based on the geodesic criterion. However, we found that the Bernoulli criterion can predict an unbound mass several times higher than the more conservative geodesic criterion. The differences are mainly caused by the usage of boundness criteria which assume some form of stationarity in regions which are still highly dynamic.

All our models are close to the threshold mass for prompt collapse to a BH, which was computed for a range of EOSs in [7] using the conformal flatness approximation, and which we could confirm in full GR for the LS220 and SHT EOSs considered here. Given that those masses exceed the maximum mass

for a uniformly rotating star, we need to ask what prevents the collapse. As it turns out, the standard notion that the prompt collapse is prevented by a differential rotation profile where the core rotates more rapidly does not apply to our models. Instead, we find an extended envelope rotating slightly below Keplerian velocity, while the core rotates more slowly than the outer layers.

We stress that envelopes are not necessarily responsible for delaying the collapse in general. However, their potential presence is an important aspect to be considered when studying the long-term stability of merger remnants. In cases where the system is stabilized not mainly by rapid rotation or temperature of the dense core, it might be less sensitive to angular momentum loss or cooling of the core. Conversely, neutrino cooling and magnetic fields might have a stronger impact on the envelopes than on the dense cores. Of course, the impact of thermal effects on the core depends on the EOS and the mass. Using a simplified analytic EOS and an idealized cooling mechanism, the BNS merger simulation presented in [5] suggests that cooling can reduce the lifetime of HMNSs. For nuclear physics EOS, the influence of thermal effects on the stability of isolated massive stars tends to be weak, see [27, 49]. On the other hand, those studies do not take into ac-

count extended envelopes, leaving room for thermally induced collapse for such systems.

ACKNOWLEDGMENTS

We would like to thank A. Bauswein, H.T. Janka, N. Stergioulas, and K. Takami for helpful discussions, and especially thank J. A. Font for carefully reading the manuscript and help with the introduction. Further, we acknowledge discussions with L. Rezzolla on the project, in particular on the HMNS density profile. This work was granted access to the HPC resources of the Rechenzentrum Garching (*Hydra* supercomputer) made available within the Distributed European Computing Initiative by the PRACE-2IP, receiving funding from the European Community's Seventh Framework Programme (FP7/2007-2013) under grant agreement number RI-283493. Part of the numerical computations were also carried out on the *Datura* cluster at the AEI. W.K. was supported by the Deutsche Forschungsgemeinschaft Grant SFB/Transregio 7. F.G. was supported by the Helmholtz International Center for FAIR within the framework of the LOEWE program launched by the State of Hesse.

-
- [1] L. Baiotti, B. Giacomazzo, and L. Rezzolla, *Phys. Rev. D* **78**, 084033 (2008).
- [2] N. Stergioulas, A. Bauswein, K. Zagkouris, and H.-T. Janka, *Mon. Not. R. Astron. Soc.* **418**, 427 (2011).
- [3] Y. Sekiguchi, K. Kiuchi, K. Kyutoku, and M. Shibata, *Phys. Rev. Lett.* **107**, 051102 (2011).
- [4] K. Hotokezaka, K. Kyutoku, H. Okawa, M. Shibata, and K. Kiuchi, *Phys. Rev. D* **83**, 124008 (2011).
- [5] V. Paschalidis, Z. B. Etienne, and S. L. Shapiro, *Phys. Rev. D* **86**, 064032 (2012).
- [6] A. Bauswein, H.T. Janka, and R. Oechslin, *Phys. Rev. D* **82**, 084043 (2010).
- [7] A. Bauswein, T. W. Baumgarte, and H.-T. Janka, *Phys. Rev. Lett.* **111**, 131101 (2013).
- [8] A. Bauswein, S. Goriely, and H.-T. Janka, *Astrophys. J.* **773**, 78 (2013).
- [9] K. Hotokezaka, K. Kiuchi, K. Kyutoku, H. Okawa, Y.-i. Sekiguchi, M. Shibata, and K. Taniguchi, *Phys. Rev. D* **87**, 024001 (2013).
- [10] K. Hotokezaka, K. Kiuchi, K. Kyutoku, T. Muranushi, Y.-i. Sekiguchi, M. Shibata, and K. Taniguchi, *Phys. Rev. D* **88**, 044026 (2013).
- [11] K. Takami, L. Rezzolla, and L. Baiotti, *Physical Review Letters* **113**, 091104 (2014).
- [12] T. W. Baumgarte, S. L. Shapiro, and M. Shibata, *Astrophysical Journal Lett.* **528**, L29 (2000).
- [13] G. M. Harry *et al.*, *Class. Quantum Grav.* **27**, 084006 (2010).
- [14] T. Accadia *et al.*, *Class. Quantum Grav.* **28**, 114002 (2011).
- [15] Y. Aso, Y. Michimura, K. Somiya, M. Ando, O. Miyakawa, T. Sekiguchi, D. Tatsumi, and H. Yamamoto, *Phys. Rev. D* **88**, 043007 (2013).
- [16] A. Bauswein and H.-T. Janka, *Phys. Rev. Lett.* **108**, 011101 (2012).
- [17] A. Bauswein, N. Stergioulas, and H.-T. Janka, *Phys. Rev. D* **90**, 023002 (2014).
- [18] P. B. Demorest, T. Pennucci, S. M. Ransom, M. S. E. Roberts, and J. W. T. Hessels, *Nature* **467**, 1081 (2010).
- [19] J. Antoniadis, P. C. C. Freire, N. Wex, T. M. Tauris, R. S. Lynch, M. H. van Kerkwijk, M. Kramer, C. Bassa, V. S. Dhillon, T. Driebe, J. W. T. Hessels, V. M. Kaspi, V. I. Kondratiev, N. Langer, T. R. Marsh, M. A. McLaughlin, T. T. Pennucci, S. M. Ransom, I. H. Stairs, J. van Leeuwen, J. P. W. Verbiest, and D. G. Whelan, *Science* **340**, 1233232 (2013).
- [20] P. Tsatsin and P. Marronetti, *Phys. Rev. D* **88**, 064060 (2013).
- [21] S. Bernuzzi, T. Dietrich, W. Tichy, and B. Brügmann, *Phys. Rev. D* **89**, 104021 (2014).
- [22] W. Kastaun, F. Galeazzi, D. Alic, L. Rezzolla, and J. A. Font, *Phys. Rev. D* **88**, 021501 (2013).
- [23] W. Tichy, *Phys. Rev. D* **84**, 024041 (2011).
- [24] M. Shibata, K. Taniguchi, and K. Uryu, *Phys. Rev. D* **71**, 084021 (2005).
- [25] D. M. Siegel, R. Ciolfi, A. I. Harte, and L. Rezzolla, *Phys. Rev. D* **87**, 121302 (2013).
- [26] K. Kiuchi, K. Kyutoku, Y. Sekiguchi, M. Shibata, and T. Wada, *Phys. Rev. D* **90**, 041502 (2014).
- [27] F. Galeazzi, W. Kastaun, L. Rezzolla, and J. A. Font, *Phys. Rev. D* **88**, 064009 (2013).
- [28] D. Alic, W. Kastaun, and L. Rezzolla, *Phys. Rev. D* **88**, 064049 (2013).
- [29] J. A. Font, *Living Rev. Relativ.* **6**, 4; <http://www.livingreviews.org/lrr> (2008).
- [30] D. Brown, P. Diener, O. Sarbach, E. Schnetter, and M. Tiglio, *Phys. Rev. D* **79**, 044023 (2009).
- [31] F. Löffler, J. Faber, E. Bentivegna, T. Bode, P. Diener, R. Haas, I. Hinder, B. C. Mundim, C. D. Ott, E. Schnetter, G. Allen, M. Campanelli, and P. Laguna, *Class. Quantum Grav.* **29**, 115001 (2012).
- [32] T. Nakamura, K. Oohara, and Y. Kojima, *Prog. Theor. Phys.*

- Suppl. **90**, 1 (1987).
- [33] M. Shibata and T. Nakamura, *Phys. Rev. D* **52**, 5428 (1995).
- [34] T. W. Baumgarte and S. L. Shapiro, *Phys. Rev. D* **59**, 024007 (1998).
- [35] D. Alic, C. Bona-Casas, C. Bona, L. Rezzolla, and C. Palenzuela, *Phys. Rev. D* **85**, 064040 (2012).
- [36] C. Bona, J. Massó, E. Seidel, and J. Stela, *Phys. Rev. Lett.* **75**, 600 (1995).
- [37] M. Alcubierre, B. Brügmann, P. Diener, M. Koppitz, D. Pollney, E. Seidel, and R. Takahashi, *Phys. Rev. D* **67**, 084023 (2003).
- [38] E. Schnetter, S. H. Hawley, and I. Hawke, *Class. Quantum Grav.* **21**, 1465 (2004).
- [39] J. Thornburg, *Classical Quantum Gravity* **21**, 743 (2004).
- [40] A. Ashtekar and B. Krishnan, *Living Rev. Relativ.* **7**, 10 (2004).
- [41] O. Dreyer, B. Krishnan, D. Shoemaker, and E. Schnetter, *Phys. Rev. D* **67**, 024018 (2003).
- [42] C. Reisswig and D. Pollney, *Classical and Quantum Gravity* **28**, 195015 (2011).
- [43] E. Gourgoulhon, P. Grandclement, K. Taniguchi, J.-A. Marck, and S. Bonazzola, *Phys. Rev. D* **63**, 064029 (2001).
- [44] N. Stergioulas and J. L. Friedman, *Astrophys. J.* **444**, 306 (1995).
- [45] J. M. Lattimer and F. D. Swesty, *Nucl. Phys. A* **535**, 331 (1991).
- [46] F. Tondeur, M. Brack, M. Farine, and J. M. Pearson, *Nuclear Physics A* **420**, 297 (1984).
- [47] G. Shen, C. J. Horowitz, and S. Teige, *Physical Review C* **82**, 015806 (2010).
- [48] G. Shen, C. J. Horowitz, and S. Teige, *Physical Review C* **83**, 035802 (2011).
- [49] J. D. Kaplan, C. D. Ott, E. P. O'Connor, K. Kiuchi, L. Roberts, and M. Duez, *Astrophys. J.* **790**, 19 (2014).
- [50] W. Kastaun, B. Willburger, and K. D. Kokkotas, *Phys. Rev. D* **82**, 104036 (2010).
- [51] R. Oechslin, S. Rosswog, and F.-K. Thielemann, *Phys. Rev. D* **65**, 103005 (2002).
- [52] C. Messenger, K. Takami, S. Gossan, L. Rezzolla, and B. S. Sathyaprakash, *Phys. Rev. X* **4**, 041004 (2014).
- [53] S. Bernuzzi, A. Nagar, S. Balmelli, T. Dietrich, and M. Ujevic, *Physical Review Letters* **112**, 201101 (2014).